nature photonics

Article

https://doi.org/10.1038/s41566-024-01387-1

In vivo ultrasound-induced luminescence molecular imaging

Received: 1 March 2023

Accepted: 8 January 2024

Published online: 16 February 2024

Check for updates

Youjuan Wang[1], Zhigao Yi[2], Jing Guo[1], Shiyi Liao[1], Zhe Li[1], Shuai Xu[1], Baoli Yin[1], Yongchao Liu[1], Yurong Feng[1], Qiming Rong[1], Xiaogang Liu[2], Guosheng Song[1] ✉, Xiao-Bing Zhang[1] ✉ & Weihong Tan[1,3] ✉

Optical imaging is crucial to study biological or pathological processes and diagnose diseases. However, poor tissue penetration typically limits conventional optical imaging. Here we report an imaging technique that uses ultrasound to activate luminescent molecules or nanoparticles through two-step intraparticle energy conversion. Ultrasonic activation can convert mechanical fluctuations into chemical energy via the piezoelectric effect and then induce luminescence via the chemiluminescent effect. We demonstrate two modalities for ultrasound-induced luminescence imaging: one achieves delayed imaging after cessation of the ultrasonic excitation, and the other enables real-time imaging during the ultrasonic excitation. Our imaging modality offers an improvement in luminescence intensity of up to 2,000-fold compared with sonoluminescence of H_2O, a 10-fold improved of signal-to-noise ratio compared with fluorescence imaging, a spatial resolution of 1.46 mm and tissue penetration of up to 2.2 cm. We demonstrate its applicability for imaging subcutaneous and orthotopic tumours, mapping lymph nodes and screening peritoneal metastatic tumours. Furthermore, we design analyte-activatable luminescence probes based on resonance energy transfer, which can assess drug-induced hepatotoxicity and distinguish the responsivity of tumours after drug treatment. We expect that our technique will enable further preclinical and clinical applications, such as the study of histopathological lesions in living animals, the early detection of tumours, the profiling of biological molecules and the monitoring of cancer treatment or prognosis, among others.

Molecular imaging is a non-invasive tool utilized for visualizing and quantifying molecular and cellular biological processes, facilitating the detection, diagnosis, prediction and monitoring of diseases[1–6]. Optical imaging, an integral component of molecular imaging, offers advantages in terms of sensitivity, specificity and real-time detection[7–11]. Currently, luminescence is generated in molecules or materials through various means such as light excitation, chemical/biochemical interactions, radionuclides or X-rays[7,12–15]. However, fluorescence imaging, which relies on real-time light excitation, often suffers from tissue autofluorescence, compromising both sensitivity and specificity in living organisms[16,17]. By contrast, other forms of luminescence imaging, such as chemiluminescence, bioluminescence, Cerenkov luminescence or X-ray-activated luminescence, can eliminate autofluorescence from biological tissues[18]. Nevertheless, bioluminescent or chemiluminescent

[1]State Key Laboratory for Chemo/Biosensing and Chemometrics, College of Chemistry and Chemical Engineering, Hunan University, Changsha, China. [2]Department of Chemistry, National University of Singapore, Singapore, Singapore. [3]The Cancer Hospital of the University of Chinese Academy of Sciences (Zhejiang Cancer Hospital), Hangzhou Institute of Medicine (HIM), Chinese Academy of Sciences, Hangzhou, China.
✉e-mail: songgs@hnu.edu.cn; songguosheng12@sina.com; xbzhang@hnu.edu.cn; tan@hnu.edu.cn

signals are often influenced by enzyme microenvironments or substrate biodistributions in living animals[19]. Cerenkov luminescence or X-ray-activated luminescence imaging typically requires high doses of radioisotopes or X-rays to achieve adequate imaging contrast, which may cause damage to normal tissue[12,20].

Ultrasound imaging is a widely accessible, cost-effective, real-time, non-invasive and safe modality that utilizes sound waves to visualize the interior of the human body with a nature similar to that of non-ionizing radiation, making it commonly used for anatomical and functional imaging in clinical settings[21–23]. Given these benefits, ultrasound waves possess the potential to serve as an energy source for activating luminescence. Sonoluminescence, a phenomenon characterized by weak light emission resulting from the cavitation of liquid under high-intensity ultrasound, has been the subject of study since 1934[24–26]. However, sonoluminescence was not deemed to be an effective imaging technique due to its low efficacy and intensity of luminescence, prolonged exposure time and extremely short lifetime[25,27,28]. To enhance ultrasound-induced luminescence intensity, chemiluminescent substrates such as luminol were used to react with reactive oxygen species (ROS) generated by ultrasonic cavitation, although the luminescence intensity remained relatively low[29–33]. In addition, the underlying mechanism of ultrasound-induced luminescence and the design of molecules specifically tailored for this purpose still lack a comprehensive understanding, indicating that ultrasound-triggered luminescence in biomedical applications remains in its early stages of development[34–37].

In this study we present a novel ultrasound-induced luminescence imaging technique that utilizes a two-step energy-conversion process to enhance the luminescence intensity, and we demonstrate its application for in vivo imaging. We convert 15 types of luminescent molecule into water-soluble nanoparticles and establish two imaging models for collecting ultrasound-induced photons: delayed ultrasound-induced luminescence imaging and real-time ultrasound-induced luminescence imaging. By leveraging the piezoelectric effect and piezocatalysis of nanoparticles, we greatly improve the ultrasound-induced luminescence intensity. Among the nanoparticles tested, trianthracene derivative-based nanoparticles (TD NPs) exhibit the highest luminescence intensity in delayed ultrasound-induced luminescence imaging. TD NPs generate polarization charges through the piezoelectric effect and subsequently produce a large amount of ROS through piezocatalysis. The generated ROS react further with the TD molecules to emit photons via a chemiluminescent process. Compared with fluorescence imaging, ultrasound-induced luminescence imaging shows both improved sensitivity and signal-to-noise ratio due to the absence of crosstalk between ultrasonic excitation and optical signal emission, resulting in a minimal background signal in both the delayed and real-time imaging modes. We successfully demonstrate the feasibility of the in vivo imaging of subcutaneous and orthotopic tumours, peritoneal metastasis tumours and lymph nodes using ultrasound-induced luminescence imaging. In addition, we showcase the in vivo molecular imaging of enzymes and reactive species during immunotherapy or drug-induced hepatotoxicity using activatable ultrasound-induced luminescence probes.

Results

Screening molecules and designing nanoparticles for ultrasound-induced luminescence imaging

We synthesized water-soluble nanoparticles by converting 15 different types of luminescent molecule, which include porphyrins, BODIPY, cyanine, trianthracene derivatives, A–D–A′–D–A conjugation molecules (where D is an electron donor and A is an electron acceptor) and semiconducting polymers, using surfactants (Fig. 1a,c, Supplementary Table 1 and Supplementary Figs. 1–5). The absorption and fluorescence spectra of these nanoparticles were characterized (Supplementary Figs. 6 and 7). Transmission electron microscopy (TEM) images and dynamic light scattering analysis confirmed that the TD NPs exhibited a spherical morphology with a narrow size distribution of approximately 30–40 nm (Fig. 1d and Supplementary Fig. 8).

To collect ultrasound-induced luminescence photons, we established new imaging apparatus as depicted in Fig. 1b and Extended Data Fig. 1, and as described in the Supplementary Methods. Two modes of ultrasound-induced luminescence imaging were implemented: delayed luminescence imaging after the cessation of ultrasonic excitation; and real-time luminescence imaging during ultrasonic excitation. In the delayed imaging mode, the ultrasonic transducer was positioned under/in the solution samples or on the tissue surface of animals to excite the nanoparticles using ultrasonic coupling gel. Immediately after the ultrasonic excitation was stopped, the samples or animals were transferred to an imaging dark box, and images were acquired using a cooled CCD (charge-coupled device) camera without light excitation (from an IVIS Lumina XR imaging system). In the real-time imaging mode, the ultrasonic transducer was placed inside the imaging dark box, and the samples were excited by ultrasonic waves inside the dark box. Ultrasound-induced luminescence images were simultaneously acquired without the need to transfer the samples.

Initially, we investigated the delayed ultrasound-induced luminescence of the nanoparticles using ultrasonic excitation. The images revealed ultrasound-induced luminescence photon emission from various nanoparticles, except for the curcumin- and IR780-based nanoparticles. Porphyrin-based nanoparticles (Ce6 and F-PpIX) exhibited a higher luminescence intensity compared with the BODIPY- and cyanine-based nanoparticles (ICG and HD). Among the semiconducting polymer-based nanoparticles, those based on PFODBT displayed the highest luminescence intensity. Notably, the TD NPs demonstrated the strongest luminescence intensity among all of the tested nanoparticles. The luminescence intensity of the TD NPs was higher than that of H_2O, PFODBT- and Ce6-based nanoparticles, with increases of 2,389.6-fold, 71.6-fold and 71.3-fold, respectively (Fig. 1e,f).

Subsequently, we collected the real-time ultrasound-induced luminescence from the nanoparticles during ultrasonic excitation. TD NPs, porphyrin-based nanoparticles and PFODBT-based nanoparticles exhibited a stronger luminescence intensity compared with the other nanoparticles. Once again, the TD NPs displayed the highest luminescence intensity among the tested nanoparticles, with an increase of 1,428.1-fold compared with H_2O (Fig. 1g). In addition, fluorescence images and intensities were obtained under appropriate excitation in the fluorescence mode (Fig. 1e,h).

Investigation of ultrasound-induced luminescence imaging

We focused on studying the luminescence performance of the TD NPs using the delayed ultrasound-induced luminescence imaging mode, which involved imaging after the cessation of ultrasonic excitation. After optimizing the surfactant, we found that TD NPs coated with DSPE-PEG (1,2-distearoyl-sn-glycero-3-phosphoethanolamine-N-[methoxy (polyethylene glycol)) exhibited the highest luminescence intensity (Supplementary Fig. 9). Subsequently, we pre-excited the TD NPs with ultrasound at different frequencies (that is, 30, 40, 50 and 100 kHz) and observed similar luminescence spectra with a peak at 625–650 nm, which was consistent with the fluorescence spectra (Fig. 2a). As the ultrasonic excitation duration was increased, the luminescence intensity of the TD NPs also increased continuously, reaching a maximum at 90 s (Fig. 2b). Similarly, an increase in the ultrasonic excitation power density led to an increased luminescence intensity of the TD NPs (Fig. 2c). Moreover, the ultrasound-induced luminescence intensity of the TD NPs showed a positive linear relationship with the nanoparticle concentration (Fig. 2d). After the cessation of ultrasonic excitation, we observed long-lasting signals from the TD NPs for over 7 h, with a half-life of approximately 180 s (Supplementary Fig. 10). To assess the tissue penetration depth of the ultrasound-induced luminescence

https://doi.org/10.1038/s41566-024-01387-1

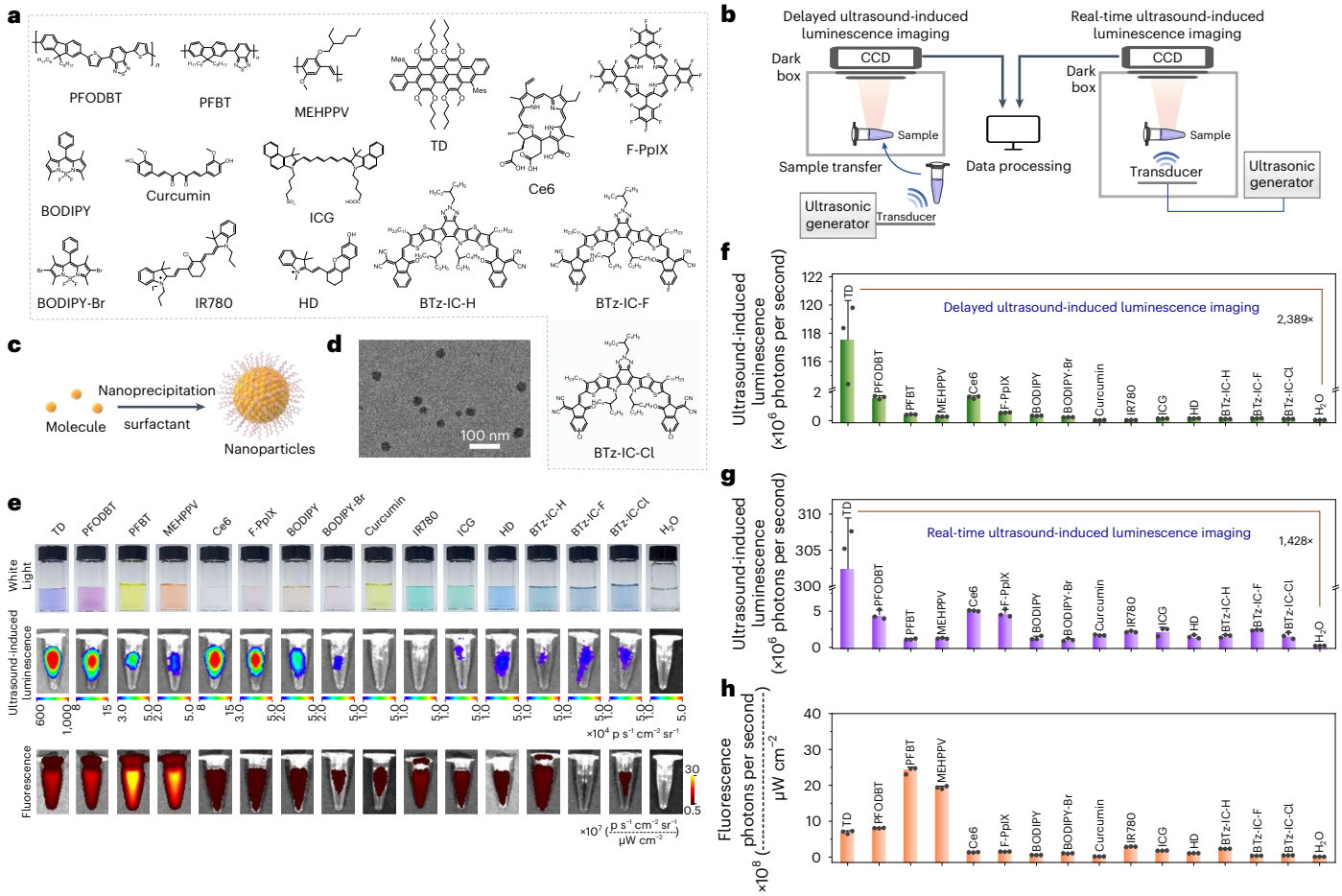

Fig. 1 | Synthesis and measurement of luminescent nanoparticles for ultrasound-induced luminescence imaging. a, Chemical structures of the various luminescent molecules. Mes, mesityl. **b**, Schematic diagram of the experimental apparatus for the modes of delayed ultrasound-induced luminescence imaging (left) and real-time ultrasound-induced luminescence imaging (right). **c**, Illustration of nanoparticle preparation. **d**, Representative TEM image of the TD NPs. **e**, Photographs (top), delayed ultrasound-induced luminescence images (middle) and fluorescence images (bottom) of the nanoparticles (20 μg ml^{-1}, 200 μl). For delayed ultrasound-induced luminescence imaging, the nanoparticle solutions were pre-excited with ultrasound (30 kHz, 4.5 W cm^{-2}). **f**, Quantification of the luminescence intensity for various nanoparticles in the delayed ultrasound-induced luminescence imaging mode in **e**. **g**, Quantification of the luminescence intensity for various nanoparticles in the real-time ultrasound-induced luminescence imaging mode during ultrasonic excitation (30 kHz, 8.7 W cm^{-2}). **h**, Quantification of the fluorescence intensity of various nanoparticles in **e**. In **f**–**h**, the data are presented as the mean ± s.d. (n = 3).

emitted from the TD NPs, we used different thicknesses of tissue and carried out testing under two modes (Supplementary Fig. 11). Although both the ultrasound-induced luminescence and fluorescence signals decreased with increasing tissue thickness, the ultrasound-induced luminescence imaging exhibited a higher signal-to-noise ratio and greater tissue penetration (up to 2.2 cm) compared with the fluorescence imaging (Fig. 2e,f and Supplementary Fig. 12). Meanwhile, we observed a decrease in the efficiency of ultrasound power transfer (η) as the tissue thickness was increased (Supplementary Fig. 13). In addition, the spatial resolution of the ultrasound-induced luminescence was assessed using full-width at half-maximum measurements, which revealed a spatial resolution of 1.46 mm with 0 mm tissue (Supplementary Fig. 14a,b).

Then, we investigated the real-time ultrasound-induced luminescence performance of the TD NPs during ultrasonic excitation, and when the ultrasonic excitation power density was increased, the luminescence intensity was enhanced (Fig. 2g). The real-time ultrasound-induced luminescence intensity of the TD NPs also increased with an increase in the nanoparticle concentration (Fig. 2h). During continuous ultrasonic excitation from 0 to 30 min, the luminescence intensity of the TD NPs gradually increased, reached a maximum at 6 min and then decreased (Supplementary Fig. 15).

Finally, we explored the potential of higher frequency ultrasound at 1 MHz and 3 MHz to stimulate luminescence, and we observed a continuous increase in the delayed ultrasound-induced luminescence intensity of the TD NPs with increasing power density of ultrasonic excitation, a longer excitation time and a higher nanoparticle concentration (Supplementary Fig. 16). Thus, the performance of ultrasound-induced luminescence of TD NPs was influenced by various factors, including the imaging mode, the excitation duration, the excitation power density, ultrasound frequency, nanoparticle surfactant and concentration, and the signal acquisition time points. However, the ultrasound-induced luminescence spectra were found to be independent of the excitation frequency.

Mechanism of ultrasound-induced luminescence

To investigate the mechanism underlying ultrasound-induced luminescence, a series of experiments was conducted. These experiments aimed to confirm the piezoelectric effect of the TD NPs, explore the generation of ROS during ultrasonic excitation, examine the chemical reactions between the TD NPs and ROS, and evaluate the resulting chemiluminescence. The piezoelectric effect of the TD NPs was confirmed by observing an increase in the open-circuit voltage when ultrasound was applied, specifically from TD molecules (Fig. 3b and Supplementary Fig. 17). Furthermore, the ultrasound-induced luminescence signal of the TD

https://doi.org/10.1038/s41566-024-01387-1

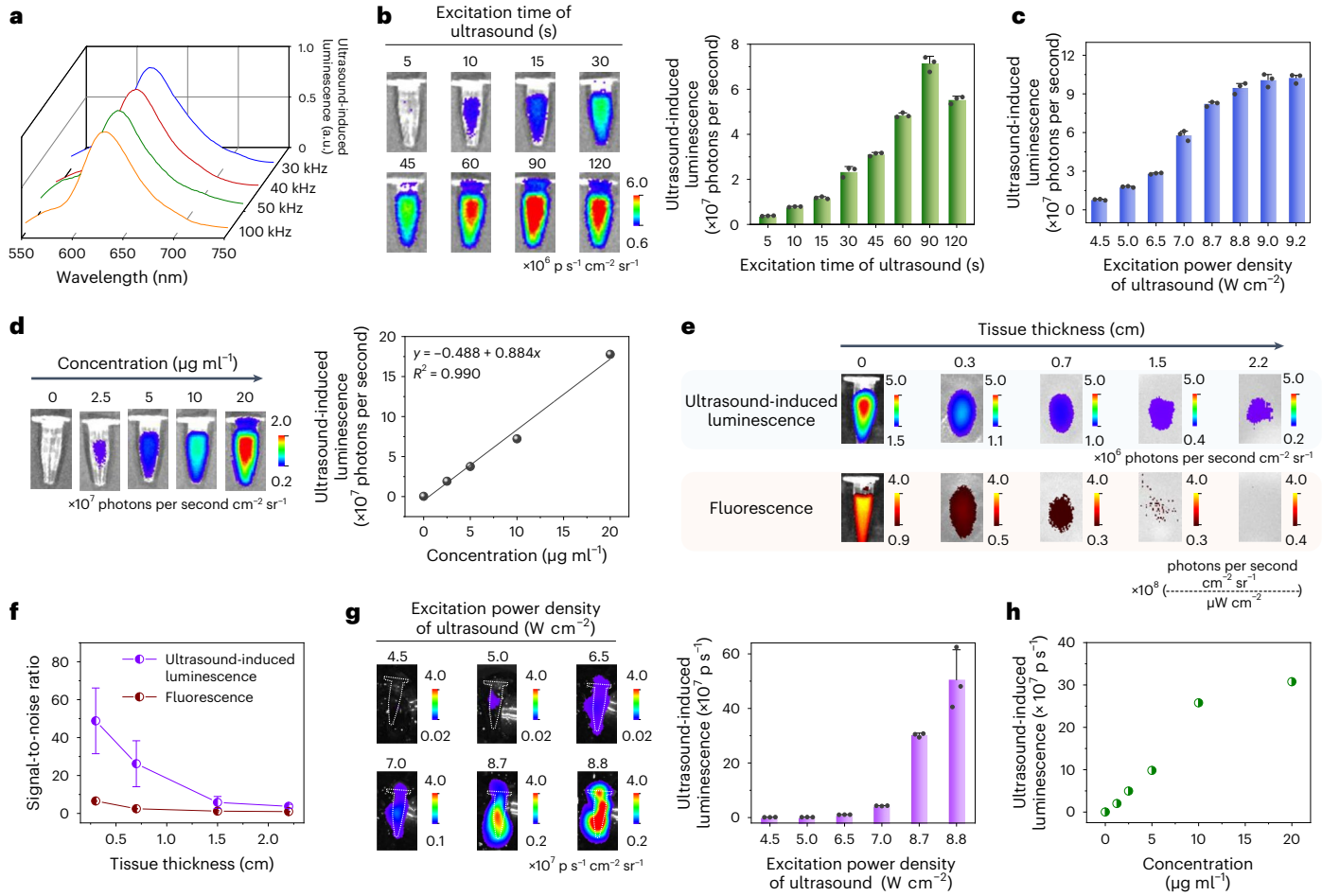

Fig. 2 | Study of the delayed ultrasound-induced luminescence imaging performance for TD NPs. a, Ultrasound-induced luminescence spectra of TD NPs excited with various ultrasound frequencies (30, 40, 50 and 100 kHz, respectively). **b**, Ultrasound-induced luminescence images (left) and intensities (right) of TD NPs (2.5 μg ml^{-1}, 200 μl) for different excitation times (30 kHz, 6.5 W cm^{-2}, 5–120 s). **c**, Ultrasound-induced luminescence intensities of TD NPs (2.5 μg ml^{-1}, 200 μl) excited with different power densities (4.5–9.2 W cm^{-2}, 30 kHz) for 30 s. **d**, Ultrasound-induced luminescence images (left) and intensities (right) of TD NPs at different concentrations, excited with ultrasound (30 kHz, 6.5 W cm^{-2}) for 15 s. *R*, coefficient of multiple correlation. **e**, Ultrasound-induced luminescence images (top) and fluorescence images (bottom) of TD NPs through tissue of different thicknesses, using test mode I shown in Supplementary Fig. 11. **f**, Signal-to-noise ratio for the ultrasound-induced luminescence and fluorescence of TD NPs as a function of the tissue thickness, using test mode I. **g**, Real-time ultrasound-induced luminescence images (left) and intensities (right) of TD NPs (20 μg ml^{-1}, 200 μl) excited at different power densities (30 kHz). **h**, Real-time ultrasound-induced luminescence intensities of TD NPs at different concentrations during ultrasonic excitation (30 kHz, 8.7 W cm^{-2}). In **b**, **c**, **f** and **g**, the data are presented as the mean ± s.d. ($n = 3$).

NPs or TD molecules was suppressed under N_2-saturated conditions compared with O_2-saturated conditions, indicating the important role of O_2 in luminescence (Fig. 3c and Supplementary Fig. 18). The decreased absorption peak of 1,3-diphenylisobenzofuran at 416 nm confirmed the production of ROS from the TD NPs (Fig. 3d and Supplementary Fig. 19). Electron spin resonance (ESR) spectra further confirmed the generation of singlet oxygen ($^1O_2$) and hydroxyl radicals (HO$^\bullet$) from the TD NPs during ultrasonic excitation (Fig. 3e and Supplementary Fig. 20). Direct incubation of $^1O_2$ and HO$^\bullet$ with the TD NPs resulted in strong chemiluminescence, and the addition of ROS radical scavengers effectively suppressed the ultrasound-induced luminescence intensity of the TD NPs, highlighting that ROS react with the TD molecules in the nanoparticles to induce chemiluminescence, whereas excess ROS diffuse out and interact with free radical scavengers (Supplementary Figs. 21 and 22). Notably, the direct heating of TD NPs to 40 °C did not result in any obvious luminescence, indicating that the observed luminescence could not be attributed to a thermal effect during ultrasonic excitation (Supplementary Fig. 23).

On the basis of the aforementioned results, a probable mechanism for ultrasound-induced luminescence was proposed (Fig. 3a). Upon ultrasonic vibration, the TD NPs generated polarization charges through the piezoelectric effect, leading to the production of $^1O_2$ and HO$^\bullet$ via piezocatalysis. These ROS then reacted with TD molecules, forming intermediates as confirmed via MALDI-TOF MS (matrix-assisted laser desorption/ionization–time of flight mass spectrometry) analysis. Oxidation of the initial TD molecules by $^1O_2$ or HO$^\bullet$ resulted in the addition of HO$^\bullet$ species and oxygen atoms, forming TD-$^\bullet$OH intermediates (**I**) or dioxetane intermediates (**II**, **III**) (with molecular weights of 1,086, 1,103 and 1,199, respectively) (Fig. 3f and Supplementary Figs. 24 and 25). These dioxetane intermediates (**II**, **III**) gradually underwent cleavage, whereas the TD-$^\bullet$OH intermediates (**I**) reacted with O_2, leading to rupture of the C–C bond and the gradual release of chemical energy[18,38,39]. Finally, the chemical energy of the intermediates was transferred to nearby intact or destroyed TD molecules, resulting in luminescence (Supplementary Fig. 26 and Supplementary Results and discussion).

After identifying the mechanism of ultrasound-induced luminescence, we designed composite nanoparticles to enhance the weaker ultrasound-induced luminescence intensity observed in the PFODBT-based nanoparticles (PFODBT NPs) (Extended Data Figs. 2

https://doi.org/10.1038/s41566-024-01387-1

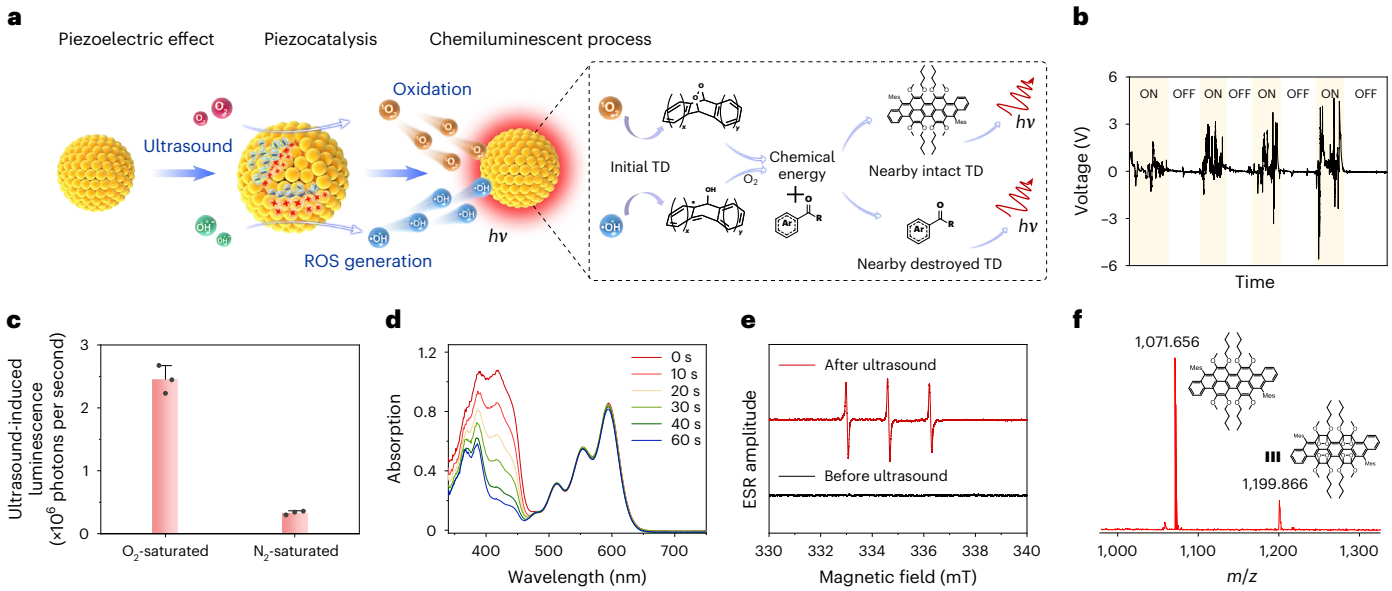

Fig. 3 | Mechanism for ultrasound-induced luminescence. a, Schematic diagram of the ultrasound-induced luminescence mechanism for TD NPs. *hν*, photon energy. **b**, Reproducible voltage output of TD when the ultrasonic transducer (30 kHz) was turned on and off. **c**, Ultrasound-induced luminescence intensity of TD NPs in water under O_2-saturated or N_2-saturated condition after ultrasonic excitation (40 kHz) for 30 s. Data are presented as the mean ± s.d. ($n = 3$). **d**, ROS generation of TD NPs as a function of the excitation time. ROS generation was determined via the degradation of 1,3-diphenylisobenzofuran at 416 nm. **e**, ESR spectra of $^1O_2$ generated from TD NPs (200 μg ml^{-1}, 100 μl) and trapped using 4-oxo-2,2,6,6-tetramethylpiperidine (1 M, 100 μl) in water before or after ultrasonic excitation. **f**, MALDI-TOF-MS spectrum of TD molecules after 30 min of ultrasonic excitation. *m/z*, mass to charge ratio.

and 3 and Supplementary Results and discussion). Various chemiluminescent substrates, such as HBA-COOH, SO, CPPO and HBA-Cl (Extended Data Fig. 2a), were doped into the PFODBT NPs. Specifically, the doping of HBA-COOH into the PFODBT NPs (PFODBT@HBA NPs) resulted in an enhancement of the luminescence intensity (121.4-fold) compared with the undoped PFODBT NPs (Extended Data Fig. 2c). In the composite nanoparticles, the piezoelectric effect of PFODBT converted the ultrasonic energy into ROS, which then reacted with HBA-COOH to generate the higher chemiluminescence intensity (Extended Data Fig. 3d–g). Similarly, doping with HBA-COOH could also increase the ultrasound-induced luminescence intensity of the BTz-IC-H-, BODIPY-Br- and PFBT-based nanoparticles (19.3-, 5.5- and 2.3-fold, respectively), following a similar principle (Supplementary Table 2 and Supplementary Fig. 27).

Ultrasound-induced luminescence imaging in vivo

Benefitting from the cytocompatibility of nanoparticles (Supplementary Fig. 28), we investigated their ability to induce luminescence under ultrasound in vivo using the delayed ultrasound-induced luminescence imaging mode, unless otherwise specified. To do this, a solution of TD NPs was placed under the abdomen of mice after ultrasonic excitation. Notably, a strong luminescence signal that was induced by ultrasound was observed from the upward side of the mice, while the fluorescence signal was barely distinguishable from the background, indicating the good penetration of ultrasound-induced luminescence in vivo (Fig. 4a). After injecting TD NPs into tumour-bearing mice, the tumour areas were excited with ultrasound and exhibited strong luminescence, while almost no background signal was detected from other parts of the mice (Fig. 4b). The signal-to-noise ratio for ultrasound-induced luminescence was calculated to be ~206, which was 11.7-fold higher than that of fluorescence (Fig. 4c and Supplementary Fig. 29). Subsequently, we intravenously injected TD NPs, and the tumour areas were excited with ultrasound at 6 h post-injection, from which there were strong luminescence signals from the tumour areas, indicating the effective tumour targeting ability of the TD NPs (Supplementary Figs. 30 and 31). In addition, the tumour areas also exhibited a strong luminescence signal during ultrasonic excitation in the real-time ultrasound-induced luminescence imaging mode (Supplementary Fig. 32).

We constructed glioblastoma multiforme (GBM) tumour model in mice and confirmed this through the haematoxylin and eosin (H&E) staining of brain slices (Fig. 4d and Supplementary Fig. 33). Upon intravenous injection of TD NPs, orthotopic GBM-bearing mice exhibited dynamically enhanced signals in their head areas after ultrasonic excitation, indicating that this imaging system can be used for deep-seated tumours (Fig. 4d and Supplementary Fig. 34). Furthermore, we used TD NPs for the ultrasound-induced luminescence imaging of pancreatic tumour-bearing mice (Fig. 4e and Supplementary Fig. 35). As time progressed, the orthotopic pancreatic tumour-bearing mice displayed a dynamic increase in the signal in the pancreas area (Fig. 4e and Supplementary Fig. 36).

Next, we used ultrasound-induced luminescence imaging for diagnosing metastatic tumours. Strong luminescent spots were detected in the intestines of tumour-bearing mice, indicating the presence of metastatic tumours, whereas no obvious signal was observed in healthy mice (Fig. 4f and Supplementary Fig. 37). The presence of metastatic tumours was further confirmed via H&E staining (Supplementary Fig. 38). By comparison, autofluorescence in the fluorescence images was so intense that it was difficult to detect metastatic tumours.

We also imaged lymph nodes by directly injecting TD NPs into the hind paws of mice (Fig. 4g). The inguinal lymph nodes displayed a strong ultrasound-induced luminescence signal and a higher signal-to-noise ratio than the fluorescence signal (Fig. 4h). Meanwhile, such ultrasound-induced luminescence could be re-excited three times with no discernible attenuation in the maximum intensity, demonstrating the capacity for multiple and longitudinal in vivo imaging sessions (Supplementary Fig. 39).

Moreover, we conducted a comprehensive investigation into the potential damage to cells and tissues under the ultrasound conditions utilized in our study, and we demonstrated that, under the tested conditions, the TD NPs exhibited negligible systemic toxicity and excellent biocompatibility (Supplementary Figs. 40–43 and Supplementary Results and discussion).

https://doi.org/10.1038/s41566-024-01387-1

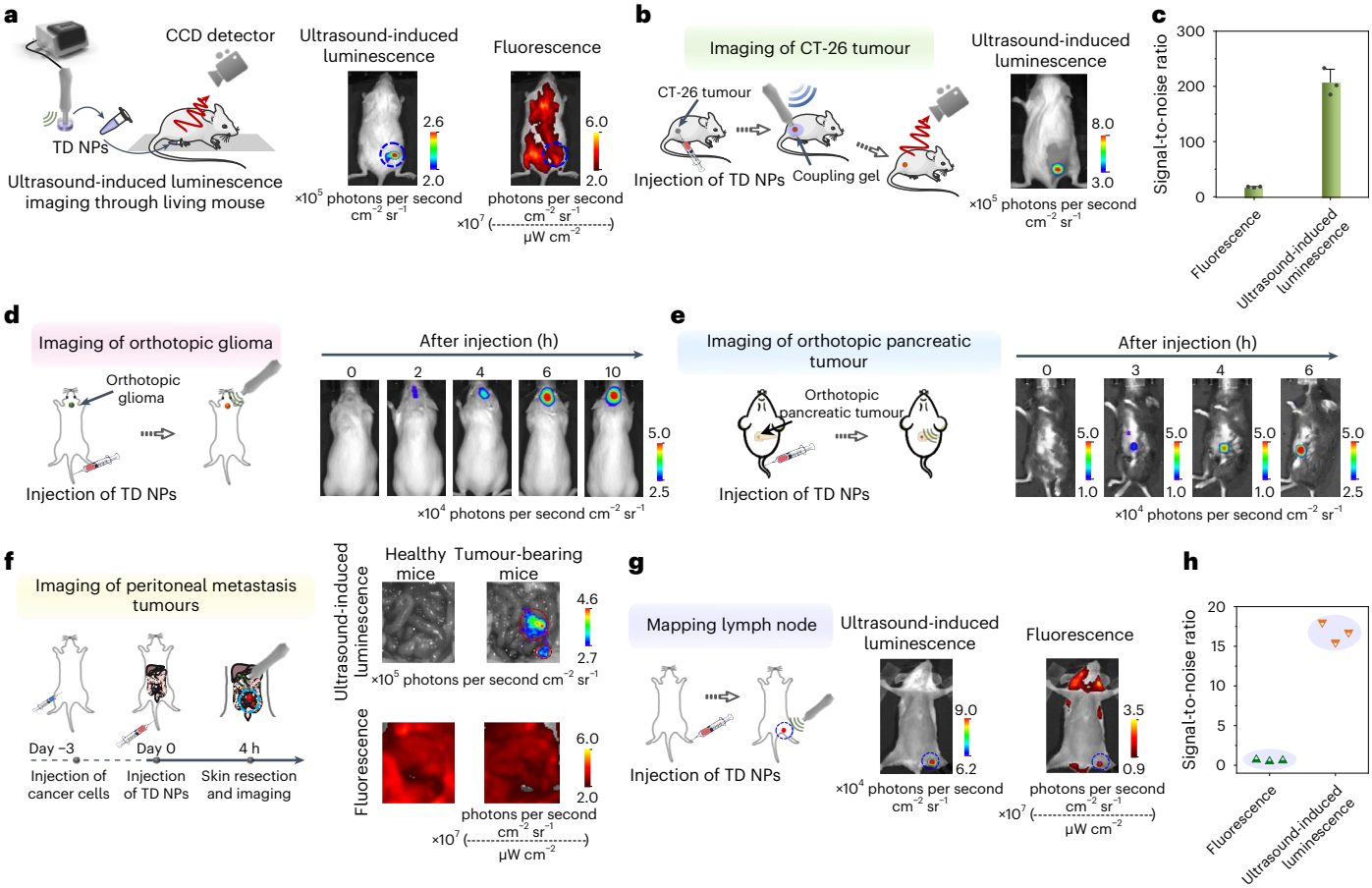

Fig. 4 | Delayed ultrasound-induced luminescence imaging in vivo. **a**, A solution of TD NPs (20 μg ml^{-1}, 200 μl) was placed under the mouse at a depth of 1.6 cm (left), and ultrasound-induced luminescence and fluorescence images (right) were collected. For fluorescence imaging: DsRed (fluorescent protein) channel, excitation at 535 nm. For delayed ultrasound-induced luminescence imaging, nanoparticles were pre-excited with ultrasound (30 kHz, 4.5 W cm^{-2}) for 15 s. **b**, Schematic diagram of the imaging of a subcutaneous CT-26 tumour (left). Ultrasound-induced luminescence image of a tumour-bearing mouse after the intratumoural injection of TD NPs (1 mg ml^{-1}, 10 μl) (right). The tumour region was pre-excited with ultrasound (30 kHz, 4.5 W cm^{-2}) for 15 s. **c**, Signal-to-noise ratio of fluorescence and ultrasound-induced luminescence in **b**. Data are presented as the mean ± s.d. ($n = 3$). $P = 2 \times 10^{-4}$. **d**, Schematic diagram of the imaging of an orthotopic glioma tumour (left), and ultrasound-induced luminescence images of glioma-bearing mice at different points after the intravenous injection of TD NPs (1 mg ml^{-1}, 200 μl) (right). The head region was pre-excited with ultrasound (1 MHz, 1.5 W cm^{-2}) for 15 s. **e**, Schematic diagram of the imaging of an orthotopic pancreatic tumour (left), and ultrasound-induced luminescence images of pancreatic tumour-bearing mice at different points after the intravenous injection of TD NPs (1 mg ml^{-1}, 200 μl) (right). The tumour region was pre-excited with ultrasound (1 MHz, 2 W cm^{-2}) for 30 s. **f**, Schematic diagram of imaging peritoneal metastatic tumours (left), and ultrasound-induced luminescence and fluorescence images of mice after skin resection to expose the abdominal cavity at 4 h after the intravenous injection of TD NPs (1 mg ml^{-1}, 200 μl) (right). The tumour regions are marked with red circles. For ultrasound-induced luminescence imaging, the tumour regions were pre-excited with ultrasound (30 kHz, 4.5 W cm^{-2}) for 15 s. **g**, Schematic diagram of imaging a lymph node (left), and ultrasound-induced luminescence and fluorescence images of the lymph node at 30 min after the intradermal injection of TD NPs (1 mg ml^{-1}, 50 μl) into the hind paw of the mouse (right). For ultrasound-induced luminescence imaging, the lymph regions were pre-excited with ultrasound (30 kHz, 4.5 W cm^{-2}) for 15 s. **h**, Signal-to-noise ratios of the lymph nodes from the fluorescence and ultrasound-induced luminescence images in **g**. $P = 2.5 \times 10^{-5}$. Statistical significance was calculated via one-way analysis of variance (ANOVA).

Activatable ultrasound-induced luminescence probes

Enzymes play a critical role in various biological processes, underscoring the importance of imaging their dynamic activities[40,41]. In this study, we propose the design of enzyme-activatable ultrasound-induced luminescence probes by incorporating different enzyme-cleavable peptide sequences as linkers between donor–acceptor pairs, on the basis of resonance energy transfer. Initially, we introduced a granzyme B-cleavable peptide sequence (Ile–Glu–Phe–Asp (IEFD)) as the linker between the TD NPs (donor) and BHQ-3 (acceptor) to create a granzyme B-activatable ultrasound-induced luminescence probe (TD-Grz-BHQ) (Fig. 5a and Supplementary Fig. 44). TD-Grz-BHQ was characterized via its absorption and fluorescence spectra. The resulting TD-Grz-BHQ probe has two absorption peaks, at 590 nm and 690 nm (Supplementary Fig. 45). Furthermore, the weak fluorescence emission from TD-Grz-BHQ confirmed the efficient luminescence quenching by BHQ-3 when spatially constrained (Fig. 5b).

Subsequently, we evaluated the performance of TD-Grz-BHQ as a sensor for the in vitro assay of granzyme B. The ultrasound-induced luminescence signals of TD-Grz-BHQ were measured after incubation with granzyme B. As expected, the IEFD peptide between the TD NPs and BHQ-3 was cleaved in the presence of granzyme B, resulting in a strong ultrasound-induced luminescence signal. This demonstrated the sensor capabilities of the TD-Grz-BHQ probe with desirable 'signal-on' behaviour (Fig. 5c and Supplementary Fig. 46). Quantification of the signals showed a linear correlation between the luminescence intensity and the granzyme B concentration (Fig. 5d). Importantly, TD-Grz-BHQ did not exhibit any obvious signal activation in the presence of other enzymes or biomolecules, confirming the probe's specificity for the detection of granzyme B (Fig. 5e).

On the basis of this resonance energy transfer, TD-Grz-BHQ can serve as a versatile platform for customizing various enzyme-responsive

https://doi.org/10.1038/s41566-024-01387-1

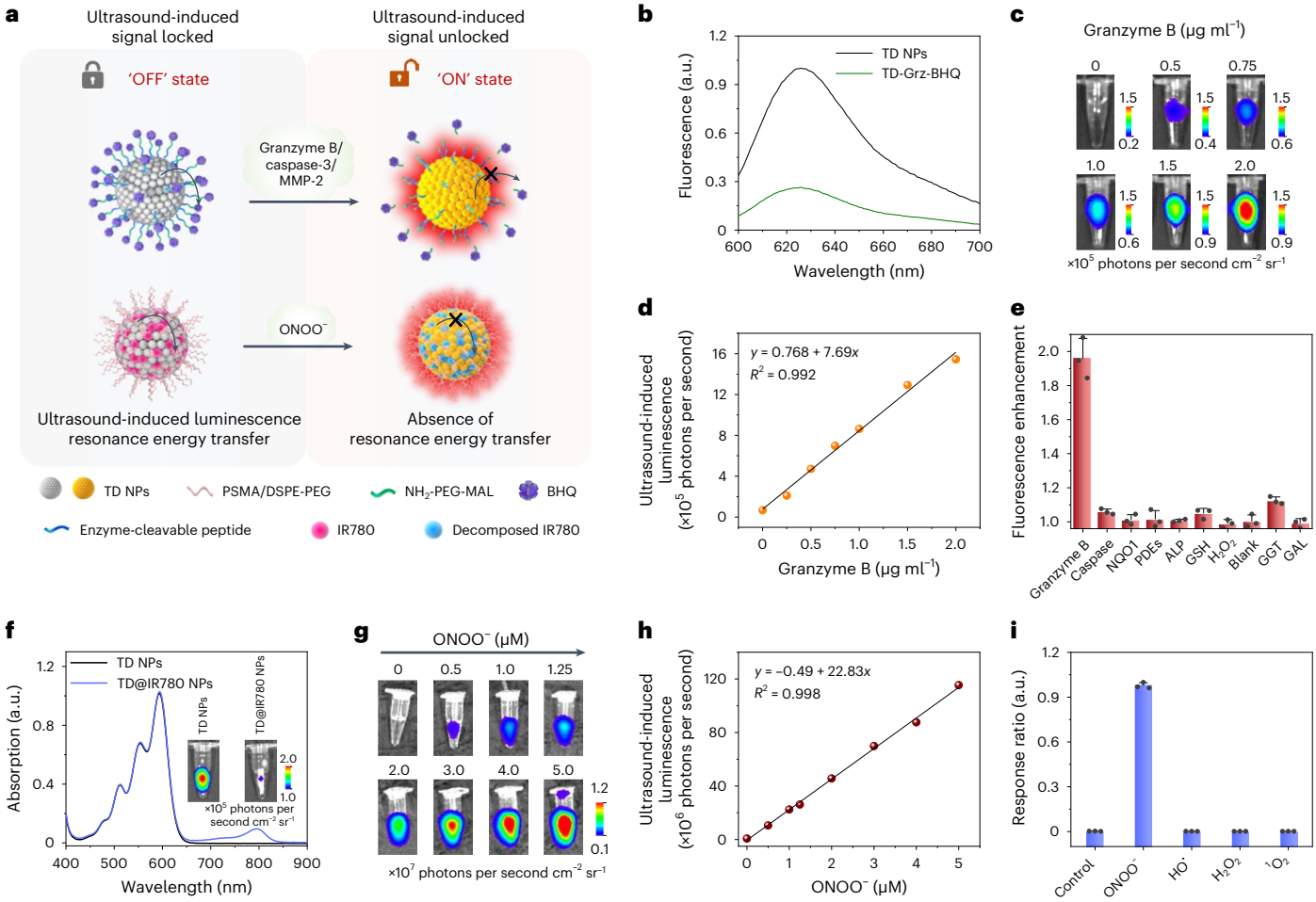

Fig. 5 | Activatable ultrasound-induced luminescence probes for imaging of enzymes and ONOO⁻. a, Schematic diagram of activatable ultrasound-induced luminescence probes for imaging of enzymes or ONOO⁻. PSMA, poly(styrene-co-maleic anhydride); MAL, maleimide. **b**, Fluorescence spectra of TD NPs and the TD-Grz-BHQ probe. **c**, Delayed ultrasound-induced luminescence imaging for TD-Grz-BHQ (1.5 μg ml^{-1}, 200 μl) in the presence of different concentrations of granzyme B. Probes were pre-excited with ultrasound at 40 kHz. **d**, Quantification of the luminescence intensity in **c**. **e**, Response ratio of TD-Grz-BHQ in the presence of various enzymes. NQO1, NAD(P)H quinone oxidoreductase 1; PDEs, phosphodiesterases; ALP, alkaline phosphatase; GSH, glutathione; GGT, γ-glutamyl transferase; GAL, β-galactosidase. **f**, Absorption spectra of TD@IR780 NPs (the peak at 450–650 nm corresponds to TD, and the peak at 780 nm corresponds to IR780). The inset shows the delayed ultrasound-induced luminescence imaging of TD NPs and TD@IR780 NPs. **g**, Delayed ultrasound-induced luminescence imaging for TD@IR780 NPs (6.25 μg ml^{-1}, 100 μl) in the presence of different concentrations of ONOO⁻. Probes were pre-excited with ultrasound at 30 kHz, 4.5 W cm^{-2}. **h**, Quantification of the luminescence intensity in **g**. **i**, Response ratio of TD@IR780 NPs in the presence of various ROS or ONOO⁻ (5 μM), where the TD@IR780 NPs showed a higher selectivity towards ONOO⁻. For **e** and **i**, the data are presented as the mean ± s.d. (n = 3).

ultrasound-induced luminescence probes. For instance, using different enzyme-cleavable peptide sequences as linkers, such as Gly–Pro–Leu–Gly–Ile–Ala (GPLGIA; a matrix metalloproteinase-2 (MMP-2)-cleavable peptide sequence) or Asp–Glu–Val–Asp (DEVD; a caspase-3-cleavable peptide sequence), we can create probes such as TD-MMP-BHQ and TD-caspase-BHQ for the detection of MMP-2 and caspase-3, respectively (Fig. 5a, Supplementary Figs. 44, 47 and 48 and Supplementary Results and discussion). In addition, we incorporated IR780 (a cyanine dye that is responsive to peroxynitrite (ONOO⁻)) into TD NPs to construct the probe TD@IR780 NPs for the imaging of ONOO⁻ through resonance energy transfer (Figs. 5a,f–i and Supplementary Results and discussion).

Ultrasound-induced luminescence imaging of granzyme B for monitoring the immune response in living mice

Cancer immunotherapy, which boosts host immunity and induces long-term immune memory effects to suppress tumour relapse and metastasis, is a vital approach for improving patient prognosis[42]. However, the immunotherapy efficacies vary widely across different tumour and treatment types[43]. The early differentiation of treated responders from non-responders would help to triage non-responding patients away from ineffective therapies[44]. However, it remains difficult to distinguish high responders from poor responders before tumour volume divergence. Granzyme B, a serine protease that is released by CD8⁺ T cells and natural killer (NK) cells during immune responses, plays a crucial role in mediating cancer cell death through cytotoxic lymphocytes[43–45]. Therefore, it is important to develop real-time and accurate imaging techniques for granzyme B to distinguish the immune response of different tumour types. In this study, we utilized TD-Grz-BHQ for imaging granzyme B and distinguishing the immune response after anti-programmed cell death ligand 1 (anti-PDL1) treatment in two tumour models (Fig. 6a). The ultrasound-induced luminescence signal of TD-Grz-BHQ was detected in CT-26 tumours after anti-PDL1 treatment. This signal was higher than the signal observed in 4T1 tumours. By contrast, tumours treated with phosphate-buffered saline (PBS) did not exhibit intense activation of luminescence signals in either the CT-26 or 4T1 tumours (Fig. 6b). From immunofluorescence staining and flow cytometry analysis of granzyme B, cytotoxic

https://doi.org/10.1038/s41566-024-01387-1

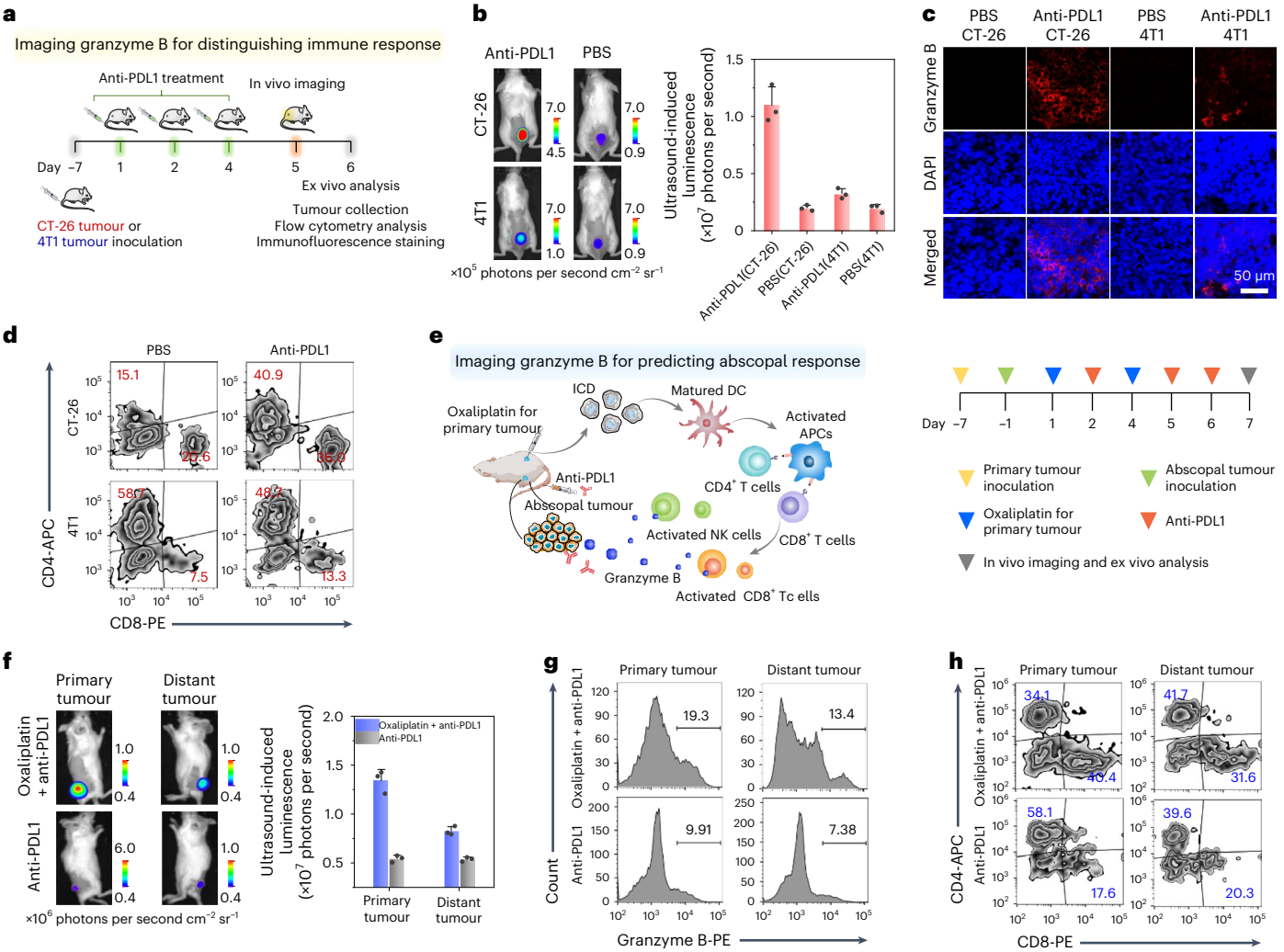

Fig. 6 | TD-Grz-BHQ activatable ultrasound-induced luminescence imaging of granzyme B in vivo. a, Schematic diagram of TD-Grz-BHQ activatable ultrasound-induced luminescence imaging, which can distinguish the immune response of different tumour types. **b**, Delayed ultrasound-induced luminescence images (left) and intensities (right) for mice from each group after injection with TD-Grz-BHQ. **c**, Confocal fluorescence images of tumour slices stained with granzyme B antibody (red colour), from each group. DAPI, 4′,6-diamidino-2-phenylindole. **d**, Flow cytometry of cytotoxic T lymphocyte ($CD8^+$ and $CD4^+$) cells within tumour tissues from each group. **e**, Schematic diagram of the abscopal effect induced by the combination of oxaliplatin and anti-PDL1 (left) and detailed administration procedures for the imaging of granzyme B after treatment (right). ICD, immunogenic cell death; DC, dendritic cell. **f**, Delayed ultrasound-induced luminescence images (left) and intensities of primary and distant tumours (right) from each group after injection with TD-Grz-BHQ. **g**, Flow cytometry of granzyme B within the tumour tissues of each group. **h**, Flow cytometry of cytotoxic T lymphocyte ($CD8^+$ and $CD4^+$) cells within the tumour tissues of each group. In **b** and **f**, the data are presented as the mean ± s.d. ($n = 3$).

T lymphocytes and NK cells confirmed that, after anti-PDL1 treatment, the CT-26 tumours showed a higher level of granzyme B, $CD8^+$ T cells and NK cells compared with the 4T1 tumours (Fig. 6c,d and Supplementary Figs. 49 and 50). The activation of ultrasound-induced luminescence signals in the tumour areas using the TD-Grz-BHQ probe was attributed to the increased release of granzyme B from activated $CD8^+$ T cells and NK cells. These findings demonstrate that TD-Grz-BHQ can not only monitor the immunotherapy response in CT-26 tumours but also distinguish the immune response between CT-26 and 4T1 tumours.

We further investigated the potential of TD-Grz-BHQ ultrasound-induced luminescence imaging for visualizing the abscopal response. The abscopal effect in oncology refers to the potential of immunotherapy not only to eliminate primary tumours but also to inhibit the growth of distant tumours[46]. However, the abscopal response may be hindered by widespread tolerance at tumour areas, making it difficult to predict the response to immunotherapy[46,47]. To address this challenge, we evaluated the abscopal response in mice receiving oxaliplatin combined with anti-PDL1 treatment using TD-Grz-BHQ ultrasound-induced luminescence imaging of the granzyme B levels. In the CT-26 tumour-bearing mice, the primary tumour was treated with either oxaliplatin or PBS, followed by the injection of anti-PDL1 and ultrasound-induced luminescence imaging (Fig. 6e). We first imaged the primary tumour and observed higher luminescence signals in the oxaliplatin-treated primary tumour compared with the PBS-treated primary tumour. Subsequently, the distant tumours in mice whose primary tumours were treated with oxaliplatin exhibited enhanced luminescence signals compared with those whose primary tumours were treated with PBS (Fig. 6f). This finding indicated that TD-Grz-BHQ can be used to monitor the granzyme B levels in both the primary and distant tumours during oxaliplatin administration combined with immune checkpoint blockade therapy. The expression level of granzyme B and the population of cytotoxic T lymphocyte cells and NK cells in the tumours were measured using immunofluorescence staining or flow cytometry analysis (Fig. 6g,h and Supplementary Fig. 51). These results demonstrated that the combination treatment (oxaliplatin for the primary tumour combined with intravenous injection of

anti-PDL1) led to increased infiltration of $CD8^+$ T cells and NK cells and higher levels of granzyme B both in the primary and distant tumours, compared with single treatment (intravenous injection of anti-PDL1). In addition, the TD@IR780 NPs probe demonstrated the ability to detect $ONOO^-$ in a drug-induced hepatotoxicity model (Supplementary Figs. 52 and 53 and Supplementary Results and discussion).

Conclusion

This study presents an advance in achieving intense and intravital ultrasound-induced luminescence imaging through a two-step intraparticle energy-conversion process. Notably, the intensity of ultrasound-induced luminescence surpasses that of sonoluminescence, while also exhibiting minimal background noise, an improved signal-to-noise ratio, imaging sensitivity and imaging depth compared with conventional fluorescence imaging. Moreover, it provides several key advantages over X-ray-activated luminescence, bioluminescence or Cerenkov luminescence, including radiation-free operation, handheld excitation, ease of use, safety and not requiring costly instrumentation.

Online content

Any methods, additional references, Nature Portfolio reporting summaries, source data, extended data, supplementary information, acknowledgements, peer review information; details of author contributions and competing interests; and statements of data and code availability are available at https://doi.org/10.1038/s41566-024-01387-1.

References

1. Chen, Y.-S. et al. Ultra-high-frequency radio-frequency acoustic molecular imaging with saline nanodroplets in living subjects. *Nat. Nanotechnol.* **16**, 717–724 (2021).
2. Jokerst, J. V. & Gambhir, S. S. Molecular imaging with theranostic nanoparticles. *Acc. Chem. Res.* **44**, 1050–1060 (2011).
3. Klinkhammer, B. M. et al. Non-invasive molecular imaging of kidney diseases. *Nat. Rev. Nephrol.* **17**, 688–703 (2021).
4. Lavine, K. J. & Liu, Y. The dynamic cardiac cellular landscape: visualization by molecular imaging. *Nat. Rev. Cardiol.* **19**, 345–347 (2022).
5. Liu, J.-n, Bu, W. & Shi, J. Chemical design and synthesis of functionalized probes for imaging and treating tumor hypoxia. *Chem. Rev.* **117**, 6160–6224 (2017).
6. Wang, Z. et al. Two-way magnetic resonance tuning and enhanced subtraction imaging for non-invasive and quantitative biological imaging. *Nat. Nanotechnol.* **15**, 482–490 (2020).
7. Jiang, Y. & Pu, K. Molecular probes for autofluorescence-free optical imaging. *Chem. Rev.* **121**, 13086–13131 (2021).
8. Zhao, Z. et al. Ultra-bright Raman dots for multiplexed optical imaging. *Nat. Commun.* **12**, 1305 (2021).
9. Kim, E. H., Chin, G., Rong, G., Poskanzer, K. E. & Clark, H. A. Optical probes for neurobiological sensing and imaging. *Acc. Chem. Res.* **51**, 1023–1032 (2018).
10. Li, Y., Gecevicius, M. & Qiu, J. Long persistent phosphors—from fundamentals to applications. *Chem. Soc. Rev.* **45**, 2090–2136 (2016).
11. Weber, J., Beard, P. C. & Bohndiek, S. E. Contrast agents for molecular photoacoustic imaging. *Nat. Methods* **13**, 639–650 (2016).
12. Pei, P. et al. X-ray-activated persistent luminescence nanomaterials for NIR-II imaging. *Nat. Nanotechnol.* **16**, 1011–1018 (2021).
13. Pratt, E. C. et al. Prospective testing of clinical Cerenkov luminescence imaging against standard-of-care nuclear imaging for tumour location. *Nat. Biomed. Eng.* **6**, 559–568 (2022).
14. Wu, X. et al. Tether-free photothermal deep-brain stimulation in freely behaving mice via wide-field illumination in the near-infrared-II window. *Nat. Biomed. Eng.* **6**, 754–770 (2022).
15. Yang, M. et al. Chemiluminescence for bioimaging and therapeutics: recent advances and challenges. *Chem. Soc. Rev.* **49**, 6800–6815 (2020).
16. Diao, S. et al. Fluorescence imaging in vivo at wavelengths beyond 1500 nm. *Angew. Chem. Int. Ed.* **54**, 14758–14762 (2015).
17. He, S., Song, J., Qu, J. & Cheng, Z. Crucial breakthrough of second near-infrared biological window fluorophores: design and synthesis toward multimodal imaging and theranostics. *Chem. Soc. Rev.* **47**, 4258–4278 (2018).
18. Miao, Q. et al. Molecular afterglow imaging with bright, biodegradable polymer nanoparticles. *Nat. Biotechnol.* **35**, 1102–1110 (2017).
19. So, M.-K., Xu, C., Loening, A. M., Gambhir, S. S. & Rao, J. Self-illuminating quantum dot conjugates for in vivo imaging. *Nat. Biotechnol.* **24**, 339–343 (2006).
20. Liu, H. et al. Intraoperative imaging of tumors using Cerenkov luminescence endoscopy: a feasibility experimental study. *J. Nucl. Med.* **53**, 1579–1584 (2012).
21. Farhadi, A., Ho, G. H., Sawyer, D. P., Bourdeau, R. W. & Shapiro, M. G. Ultrasound imaging of gene expression in mammalian cells. *Science* **365**, 1469–1475 (2019).
22. Gilad, A. A. & Shapiro, M. G. Molecular imaging in synthetic biology, and synthetic biology in molecular imaging. *Mol. Imaging Biol.* **19**, 373–378 (2017).
23. Heiles, B., Terwiel, D. & Maresca, D. The advent of biomolecular ultrasound imaging. *Neuroscience* **474**, 122–133 (2021).
24. Frenzel, H. & Schultes, H. Luminescenz im ultraschallbeschickten Wasser. *Z. Phys. Chem.* **27**, 421–424 (1934).
25. Didenko, Y. T., McNamara III, W. B. & Suslick, K. S. Molecular emission from single-bubble sonoluminescence. *Nature* **407**, 877–879 (2000).
26. Doktycz, S. J. & Suslick, K. S. Interparticle collisions driven by ultrasound. *Science* **247**, 1067–1069 (1990).
27. Barber, B. P. & Putterman, S. J. Observation of synchronous picosecond sonoluminescence. *Nature* **352**, 318–320 (1991).
28. Xing, D., He, L., Tang, Y. & Tan, S. Sonoluminescence imaging in vivo. In *Proc. SPIE 4162, Controlling Tissue Optical Properties: Applications in Clinical Study* (ed. Tuchin, V. V.) 86–92 (SPIE, 2000).
29. He, L., Xing, D., Yan, X. & Ueda, K.-I. Chemiluminescence detection from sonodynamic action in vitro and in vivo. In *Proc. SPIE 4597, Biophotonics Instrumentation and Analysis* (eds Chiou, A. E. T. et al.) 43–50 (SPIE, 2001).
30. He, L., Xing, D., Yao, Y., Yan, X. & Ueda, K.-I. Tumor detection with sonodynamic chemiluminescence from ATX-70 and FCLA under ultrasonic excitation. In *Proc. SPIE 4612, Optical Methods for Tumor Treatment and Detection: Mechanisms and Techniques in Photodynamic Therapy XI* (ed. Dougherty, T. J.) 196–203 (SPIE, 2002).
31. He, Y., Tang, Y., Tan, S. & Xing, D. FCLA-enhanced sonoluminescence imaging in vivo. In *Proc. SPIE 3863, 1999 International Conference on Biomedical Optics* (eds Luo, Q. et al.) 129–133 (SPIE, 1999).
32. He, Y., Xing, D., Tan, S., Tang, Y. & Ueda, K.-I. In vivo sonoluminescence imaging with the assistance of FCLA. *Phys. Med. Biol.* **47**, 1535–1541 (2002).
33. Wang, L. V. & Shen, Q. Sonoluminescent tomography of strongly scattering media. *Opt. Lett.* **23**, 561–563 (1998).
34. Xu, C. et al. Nanoparticles with ultrasound-induced afterglow luminescence for tumour-specific theranostics. *Nat. Biomed. Eng.* **7**, 298–312 (2022).
35. Wang, W. et al. Ultrasound triggered organic mechanoluminescence materials. *Adv. Drug Deliv. Rev.* **186**, 114343 (2022).

36. Wang, W. et al. Ultrasound-triggered in situ photon emission for noninvasive optogenetics. *J. Am. Chem. Soc.* **145**, 1097–1107 (2023).
37. Wu, X. et al. Sono-optogenetics facilitated by a circulation-delivered rechargeable light source for minimally invasive optogenetics. *Proc. Natl Acad. Sci. USA* **116**, 26332–26342 (2019).
38. Zhang, G. et al. A selective and sensitive chemiluminescence reaction of 4,4′(5′)-bis[2-(9-anthryloxy)ethylthio]tetrathiafulvalene with singlet oxygen. *Chem. Commun.*, 2072–2073 (2004).
39. Dang, J. & Zhang, Q. Gas-phase reaction of benzo[*a*]anthracene with hydroxyl radical in the atmosphere: products, oxidation mechanism, and kinetics. *J. Mol. Model.* **24**, 320 (2018).
40. Li, H. et al. Activity-based NIR fluorescent probes based on the versatile hemicyanine scaffold: design strategy, biomedical applications, and outlook. *Chem. Soc. Rev.* **51**, 1795–1835 (2022).
41. Wu, X., Li, H., Lee, E. & Yoon, J. Sensors for in situ real-time fluorescence imaging of enzymes. *Chem* **6**, 2893–2901 (2020).
42. Zhou, L., Zhang, P., Wang, H., Wang, D. & Li, Y. Smart nanosized drug delivery systems inducing immunogenic cell death for combination with cancer immunotherapy. *Acc. Chem. Res.* **53**, 1761–1772 (2020).
43. Nguyen, A. et al. Granzyme B nanoreporter for early monitoring of tumor response to immunotherapy. *Sci. Adv.* **6**, eabc2777 (2020).
44. Larimer, B. M. et al. Granzyme B PET imaging as a predictive biomarker of immunotherapy response. *Cancer Res.* **77**, 2318–2327 (2017).
45. He, S., Li, J., Lyu, Y., Huang, J. & Pu, K. Near-infrared fluorescent macromolecular reporters for real-time imaging and urinalysis *of cancer immunotherapy*. *J. Am. Chem. Soc.* **142**, 7075–7082 (2020).
46. Ngwa, W. et al. Using immunotherapy to boost the abscopal effect. *Nat. Rev. Cancer* **18**, 313–322 (2018).
47. Zhao, Y. et al. ICAM-1 orchestrates the abscopal effect of tumor radiotherapy. *Proc. Natl Acad. Sci. USA* **118**, e2010333118 (2021).

Methods

Ultrasound-induced luminescence imaging in solution

We set up new apparatus to collect the photons for ultrasound-induced luminescence imaging (details in the Supplementary Methods).

For delayed ultrasound-induced luminescence imaging after the cessation of ultrasonic excitation (30 kHz), the nanoparticle solutions were kept in 24-well plates, and the ultrasonic transducer was placed into the sample solution to excite the nanoparticles. Immediately after ultrasonic excitation, the solution samples were transferred into a dark box and the luminescence images were collected via a cooled CCD camera using an IVIS Lumina XR imaging system. The imaging parameters are as follows: bioluminescence modes; open filter; field of view, C; and an acquisition time of 10 s.

For real-time ultrasound-induced luminescence imaging during ultrasonic excitation, the ultrasonic transducer was set up in the dark box and placed on tubes containing solution samples to excite the nanoparticles using an ultrasonic coupling gel. The luminescence images were collected during ultrasonic activation via cooled CCD camera, using an IVIS Lumina XR imaging system. The imaging parameters are as follows: bioluminescence modes; open filter; field of view, C; and an acquisition time of 1 s.

For delayed ultrasound-induced luminescence imaging after the cessation of higher frequency ultrasound at 1 MHz and 3 MHz, this was carried out by placing the nanoparticle solutions in glass bottles and positioning the ultrasonic transducer beneath the solution sample for nanoparticle excitation. Subsequently, the solution samples were transferred into the dark box immediately after ultrasonic excitation, and luminescence images were acquired using the IVIS Lumina XR imaging system. The imaging parameters are as follows: bioluminescence modes; open filter; field of view, C; and an acquisition time of 10 s.

Ultrasound-induced luminescence imaging and fluorescence imaging in vivo

After various administrations, the above mice were anaesthetised using 2% isoflurane in oxygen. The mice were pre-excited with either 30 kHz or 1 MHz ultrasound, and ultrasonic coupling gel was applied between the ultrasonic transducer and the region of interest (ROI). Immediately after ultrasonic excitation, the mice were transferred into the dark box and the luminescence images were collected via the cooled CCD camera using the IVIS Lumina XR imaging system. The imaging parameters are as follows: bioluminescence modes; open filter; field of view, C; and an acquisition time of 10 s or 30 s.

For real-time ultrasound-induced luminescence imaging during ultrasonic excitation, the ultrasonic transducer was set up in a dark box and placed onto the tumours of the mice using ultrasonic coupling gel. The ultrasound-induced luminescence images were collected during ultrasonic activation (30 kHz, 8.7 W cm^{-2}), via the cooled CCD camera, using the IVIS Lumina XR imaging system. The imaging parameters are as follows: bioluminescence modes; open filter; field of view, C; and an acquisition time of 1 s.

The fluorescence images were collected using the IVIS Lumina XR imaging system. The imaging parameters are as follows: fluorescence modes; acquisition time of 1 s; excitation at 535 nm; emission, DsRed channel; and field of view, C.

The images were analysed via ROI analysis using Living Image 4.3.1 software[18].

The signal-to-noise ratio was calculated as the ratio of the luminescence intensity (ultrasound-induced luminescence imaging or fluorescence imaging) from the ROI containing nanoparticles to that of the tissue without nanoparticles.

Data availability

All of the data that support the findings of this study are reported in the main text and Supplementary Information. The data that support the findings of this study are available from the corresponding author upon reasonable request, and data for all figures can be found at https://doi.org/10.6084/m9.figshare.24579853. Source data are provided with this paper.

Acknowledgements

This work was supported by the National Key R&D Program of China (grant no. 2019YFA0210100 (to X.-B.Z.)) and the National Natural Science Foundation of China (grant nos U21A20287 (to G.S.) and 22234003 and 21890744 (to X.-B.Z.)).

Author contributions

J.G. and Z.L. synthesized the TD molecules. S.X. and Y.F. synthesized the HBA-COOH molecules. Y.L. synthesized the BODIPY, BODIPY-Br and HD molecules. Z.L. and B.Y. synthesized the BTz-IC-H, BTz-IC-F and BTz-IC-Cl molecules. Y.W. and S.L. conducted all experiments in solution. Y.W., S.L. and Q.R. built all of the animal models and conducted all of the animal experiments. Y.W., Z.L. and S.L. synthesized all nanoparticles. Y.W. collected the raw data in all experiments and designed the schematic diagram. G.S. conceived the idea for this project. G.S. and Y.W. designed the research and all experiments. Y.W. and G.S. analysed all of the data and interpreted the results. Y.W., G.S., X.-B.Z. and W.T. wrote the paper. G.S., X.-B.Z., W.T. and Y.W. developed the discussion. G.S. supervised all experiments. Z.Y. and X.L. helped to analyse the luminescence mechanism and wrote the paper. All authors provided critical feedback on the research and the paper.

Competing interests

The authors declare no competing interests.

Additional information

Extended data is available for this paper at https://doi.org/10.1038/s41566-024-01387-1.

Supplementary information The online version contains supplementary material available at https://doi.org/10.1038/s41566-024-01387-1.

Correspondence and requests for materials should be addressed to Guosheng Song, Xiao-Bing Zhang or Weihong Tan.

Peer review information *Nature Photonics* thanks Kanyi Pu and the other anonymous, reviewer(s) for their contribution to the peer review of this work.

https://doi.org/10.1038/s41566-024-01387-1

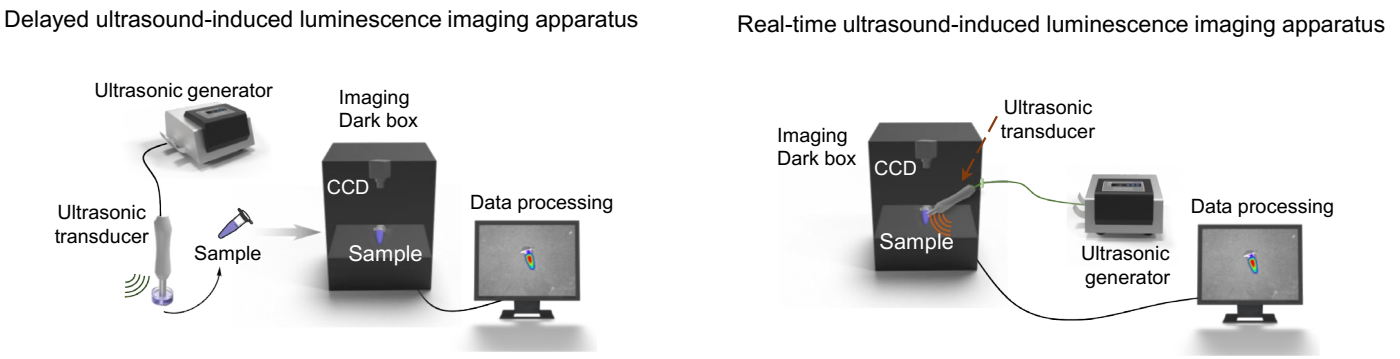

Extended Data Fig. 1 | Schematic diagram of set up apparatus for the mode of "delayed ultrasound-induced luminescence imaging" and "real-time ultrasound-induced luminescence imaging".

https://doi.org/10.1038/s41566-024-01387-1

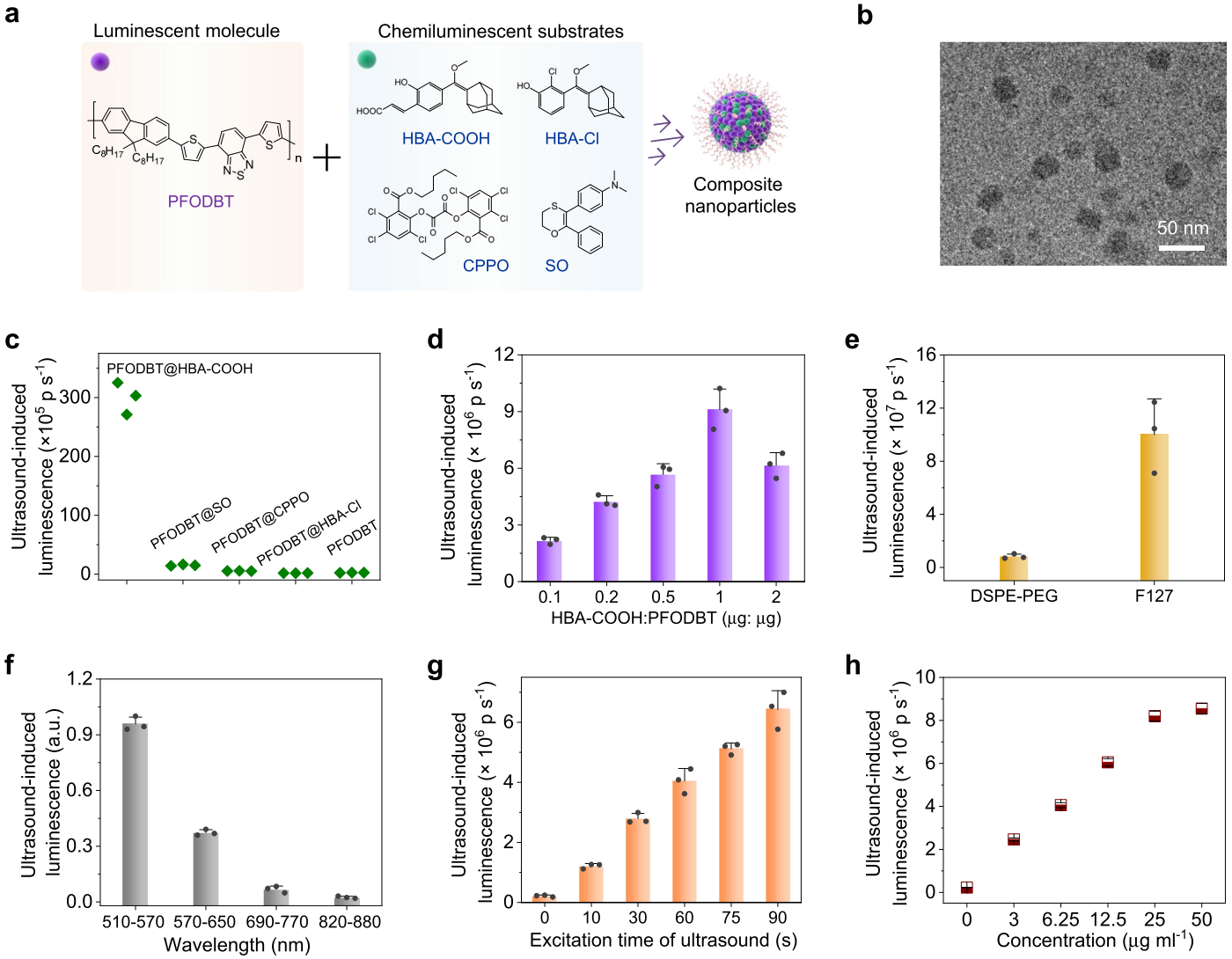

Extended Data Fig. 2 | Design of composite nanoparticles to enhance ultrasound-induced luminescence, in the mode of "delayed ultrasound-induced luminescence imaging". **a**, Schematic diagram for design of composite nanoparticles by luminescent molecule (PFODBT) and chemiluminescent substrates. **b**, TEM image revealed spherical PFODBT@HBA-NPs. **c**, Ultrasound-induced luminescence intensity of various chemiluminescent substrates doped PFODBT-NPs (50 μg mL^{-1}, 400 μL) pre-excited with ultrasound (30 kHz, 4.5 W cm^{-2}) for 45 s. **d**, Ultrasound-induced luminescence intensity of PFODBT@HBA-NPs with different ratios of HBA-COOH: PFODBT, nanoparticle solutions (50 μg/mL, 200 μL) were pre-excited with ultrasound (30 kHz, 4.5 W/cm^2) for 15 s. **e**, Ultrasound-induced luminescence intensity of PFODBT@HBA-NPs with different surfactants, those nanoparticles (50 μg mL^{-1}, 400 μL) were pre-excited with ultrasound (30 kHz, 4.5 W cm^{-2}) for 30 s. **f**, Ultrasound-induced luminescence emission of PFODBT@HBA-NPs (PFODBT: HBA-COOH = 1: 1, 25 μg mL^{-1}, 200 μL) in different channels, pre-excited with ultrasound (30 kHz, 4.5 W cm^{-2}) for 15 s. **g**, Ultrasound-induced luminescence intensity of PFODBT@HBA-NPs (6.25 μg mL^{-1}, 200 μL) after different time of ultrasonic excitation (30 kHz, 4.5 W cm^{-2}). **h**, Ultrasound-induced luminescence intensity of various concentrations of PFODBT@HBA-NPs pre-excited with ultrasound (30 kHz, 4.5 W cm^{-2}) for 15 s. Data for **d**–**g** are presented as mean values ± s.d. (n = 3).

https://doi.org/10.1038/s41566-024-01387-1

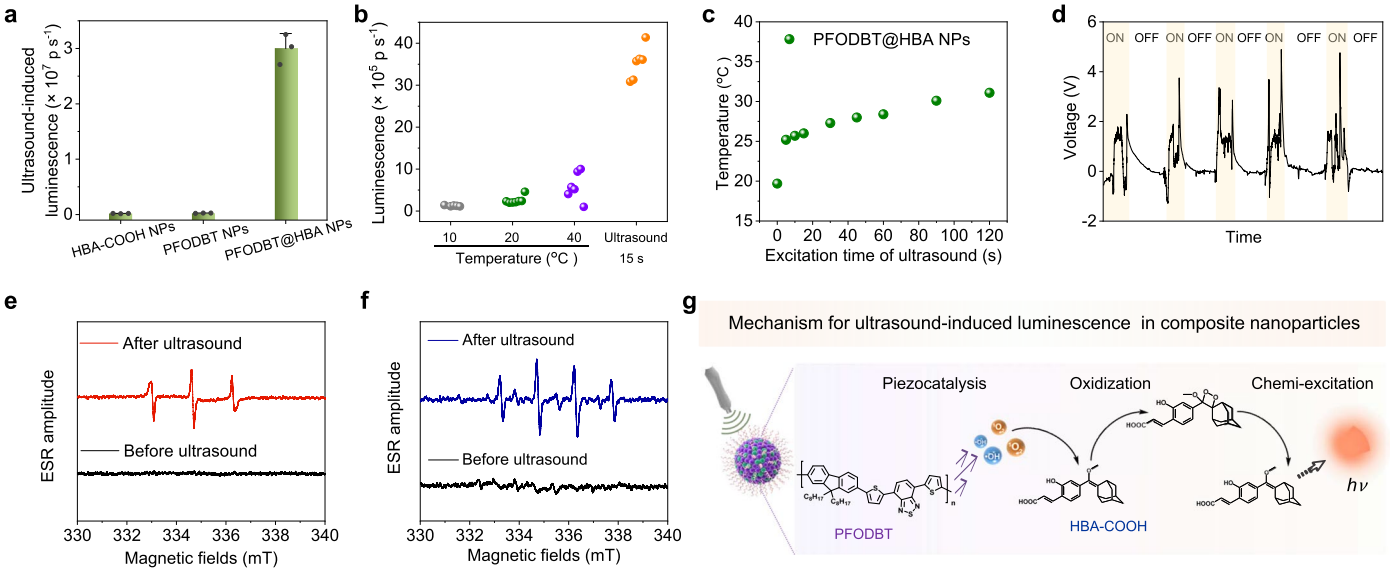

Extended Data Fig. 3 | Mechanism for ultrasound-induced luminescence of PFODBT@HBA-NPs. a, Ultrasound-induced luminescence intensity of HBA-COOH-NPs, PFODBT-NPs, PFODBT@HBA-NPs (50 μg mL^{-1}, 400 μL), pre-excited with ultrasound (30 kHz, 4.5 W cm^{-2}) for 45 s. Data are presented as mean values ± s.d. (n = 3). **b**, Luminescence intensity of PFODBT@HBA-NPs (12.5 μg mL^{-1}, 100 μL) excited by heating at various temperatures (for example, 10, 20, and 40 °C) or ultrasonic excitation (30 kHz, 4.5 W cm^{-2} for 15 s). **c**, Temperatures of PFODBT@HBA-NPs after receiving different times of ultrasonic excitation (30 kHz, 6.5 W cm^{-2}), as measured by an infrared thermal camera. **d**, Reproducible voltage output of PFODBT when the ultrasonic transducer (30 kHz) was turned on and off. **e**, ESR spectra of $^1O_2$ generated from PFODBT-NPs (200 μg mL^{-1}, 100 μL) and trapping by 4-oxo-2,2,6,6-tetramethylpiperidine (TEMP) (1 M, 100 μL) before or after ultrasonic excitation. **f**, ESR spectra of •OH generated from PFODBT-NPs (200 μg mL^{-1}, 100 μL) and trapped by dimethyl-1-pyrroline *N*-oxide (DMPO) (1 M, 100 μL) in water before or after ultrasonic excitation. **g**, Schematic diagram of ultrasound-induced luminescence mechanism for PFODBT@HBA-NPs.